Tractive performance of rigid wheel in granular media using coarse-scale DEM models

Bohumir Jelinek[a,*], Angela Card[a], George L. Mason[a], Karl Grebner[a], Aidan Dickerson[a], Thomas Skorupa[b], Michael Cole[b], Jody D. Priddy[c]

[a]*Center for Advanced Vehicular Systems, Mississippi State University, 200 Research Blvd., Mississippi State, MS 39762, USA*
[b]*U.S. Army Combat Capabilities Development Command Ground Vehicle Systems Center, 6501 East Eleven Mile Rd., Warren, MI 48397, USA*
[c]*U.S. Army Engineer Research and Development Center Geotechnical and Structures Laboratory, 3909 Halls Ferry Rd., Vicksburg, MS 39180, USA*

Abstract

Understanding interactions between wheel and granular media in variable loading conditions is critical for prediction of mobility of wheeled vehicles in off-road environments. The discrete element method (DEM) is routinely used for modeling vehicle off-road performance, but the method's accuracy is often not fully established.

In this work, the DEM modeling accuracy is assessed by the comparison of ten DEM soil models with laboratory soil-bin measurements of net traction, gross traction, and sinkage of a wheel operating in sand. Laboratory soil-bin measurements, serving as reference for DEM simulations, were taken from physical experiments by Shinone et al. (2010), examining a 165/60R13 wheel with circumferential velocity of 97.6 mm/s and vertical contact load of 980 N in varying slip conditions.

The set of ten DEM models was selected from the Generic EDEM Material Model database from Altair®'s EDEM™ software package, choosing the materials matching the bulk density and angle of repose for dry sand.

Given the large particle size and no additional calibration of the DEM models, finding overall reasonable match with the gross traction from lab measurements and identifying a material predicting the net traction with a satisfiable accuracy encourages further use, refinement, and calibration of the DEM-based soil models.

Keywords:
Off-Road Mobility, Tractive Performance, Discrete Element Method, Rigid Wheel

1. Introduction

Prediction of vehicle mobility for vehicles in off-road environment presents a challenge for agriculture, construction, military, and space exploration. Suspension and powertrain systems are usually characterized well, but the accuracy of mobility models suffers from hard-to-predict terrain response. The subgrade materials that a vehicle operates on may include rock, gravel, sand, silt, clay soil, or their mixtures with various degrees of saturation. Even relatively homogeneous subgrade is hard to model numerically at the continuum level due to large deformation and material non-linearity, as well as at the particle level due to the complex geometry of soil particles, variability in contact mechanics, and high number of degrees of freedom involved. Predictions of mobility using numerical models must therefore compromise between sufficiently detailed representation and capabilities of high-performance computing.

Multiple studies have used DEM to characterize the interaction of granular subgrades with rigid and flexible wheels. The bulk of DEM work has focused on predicting the mobility of rovers on Earth, the Moon, and Mars in regolith sediments (Nakashima et al., 2010; Knuth et al., 2012; Nakashima and Kobayashi, 2014; Johnson et al., 2015, 2017) exploring the effects of gravity on sinkage and motion resistance of a rigid rover wheel. Tractive and steering performance of off-road wheels on dry sand was analyzed by Du et al. (2017a,b, 2018). These studies examined the effects of lug type, intersection of lug bars, and central angle, with the objective to improve performance prediction for straight and steered performance. The scope of off-road mobility modeling was extended beyond rigid wheels by introducing finite element pneumatic tire model (Recuero et al., 2017). Vertical stress under the wheels of agricultural machinery obtained from DEM using Yade (Šmilauer et al., 2015) was compared with pseudo-analytical continuum model and field measurements field measurements (De Pue et al., 2019; De Pue and Cornelis, 2019; De Pue et al., 2020).

Yang et al. (2020) performed DEM-FEM (Finite Element Method) simulations of flexible multi-layer tire on gravel at 10%, 20%, and 30% slip and showed a reasonable agreement of sinkage, gross tractive effort, and tractive force with experiment. These models, however, require a careful calibration (Coetzee, 2017; Zeng et al., 2020a,b), and, in many cases, non-spherical particles are used to better match the experiments (Coetzee, 2020).

In this work, predictions from DEM simulations are compared with laboratory soil-bin measurements by Shinone et al. (2010), examining a 165/60R13 wheel with constant circumferential velocity of 97.6 mm/s and vertical contact load of 980 N operating in powered conditions under slips in the range of −5.9% to 54.8%. Simulations of a rigid wheel in particle bed

*Corresponding author

with the same dimension and under the same set of slip conditions as those used for laboratory measurements are performed using ten coarse-grain out-of-the-box DEM material models selected to mimic sand-like macroscopic properties. Values of the net traction, gross traction, and sinkage were obtained by averaging from each simulation. Effects of DEM parameters on material responses are discussed. The goal of the study is to evaluate capability of coarse-grain DEM models to predict the net traction, gross traction, and sinkage of a smooth wheel operating in sand under braked and powered conditions.

2. DEM background

A particle bed to simulate wheel-soil interactions was generated using particle-factory functionality of the Altair®'s EDEM™ software. The particle bed was assembled from five identical material blocks repeated along the longitudinal direction. Only the particles in a single block were settled under periodic boundary conditions to lower the simulation time needed to populate the bed with particles. A smooth-surface cylindrical wheel without tread was constructed from triangular facets. Fig. 1 illustrates the wheel and enclosing box while Table 1 specifies their dimensions. Nomenclature used in this work is described in Table A.4.
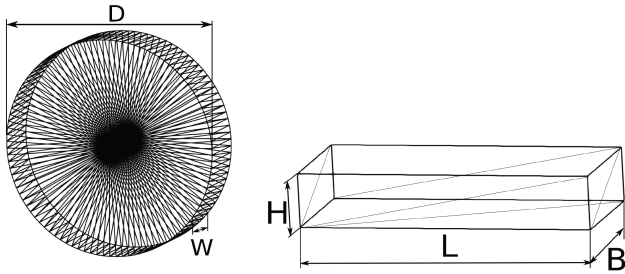

Figure 1: Triangular facet representation of the wheel and enclosing box

Table 1: Wheel and box dimensions

Property	Symbol	Units	Value
Wheel diameter	D	cm	53.49
Wheel width	W	cm	16.99
Wheel weight	F_G	N	980.33
Box length	L	cm	301.5
Box width	B	cm	48.0
Box depth	H	cm	60.5
Soil depth	h	cm	60
Number of particles	N	–	97152

Ten different DEM soil models with sand-like macroscopic response were evaluated. Models were chosen from Altair®'s EDEM™ GEMM database based on the requirements to match the dry sand: a bulk density range of 1500 to 2000 kg/m³ and an angle of repose of 34° (Glover, 1997). To represent homogeneous soil with a degree of randomness, particle sizes were

scaled to produce a normal distribution. Blocks were duplicated within particle beds and then settled to negligible kinetic energies. Table 2 presents GEMM particle properties.

Table 2: Particle Properties

	Material number				
Property[1]	1507	1301	1311	1615	1706
ν	0.25	0.25	0.25	0.25	0.25
ρ	3300	3300	3300	3300	3300
G	10	10	10	10	10
e^p	0.35	0.15	0.55	0.55	0.35
μ_s^p	0.92	0.68	0.68	1.04	1.16
μ_r^p	0	0	0	0	0
γ^p	4.5	0	0	18	0
e^g	0.5	0.5	0.5	0.5	0.5
μ_s^g	0.45	0.45	0.45	0.45	0.45
μ_r^g	0.15	0.15	0.15	0.15	0.15
γ^g	4.5	0	0	18	0
	Material number				
Property[1]	1111	1501	1308	1105	1636
ν	0.25	0.25	0.25	0.25	0.25
ρ	3300	3300	3300	3300	3300
G	10	10	10	10	10
e^p	0.55	0.35	0.35	0.15	0.75
μ_s^p	0.44	0.92	0.68	0.44	1.04
μ_r^p	0	0	0	0	0.05
γ^p	0	18	9	18	0
e^g	0.5	0.5	0.5	0.5	0.5
μ_s^g	0.45	0.45	0.45	0.45	0.45
μ_r^g	0.15	0.15	0.15	0.15	0.15
γ_g	0	18	9	18	0

[1]A superscript of p implies particle-particle interaction, while g is a particle-geometry interaction.

All particles were a multi-spherical shape. This shape is the only particle shape defined for the GEMM database. Individual spheres had a radius of 9.5 mm with a fixed overlap of 37.47% of the radius. Fig. 2 visualizes the multi-sphere particles. The

Figure 2: Multi-spherical particle shape

Hertz-Mindlin (no slip) and Hertz-Mindlin with JKR (Altair Engineering, 2022) models were used to represent DEM contact models. Hertz-Mindlin (Mindlin and Deresiewicz, 1953) is

the default model used in EDEM due to its accurate and efficient force calculation. The Hertz-Mindlin JKR model was used for particles with a non-zero JKR coefficient. For Hertz-Mindlin, the normal force is a function of normal overlap δ_n:

$$F_n = \frac{4}{3} E^* \sqrt{R^*} \delta_n^{\frac{3}{2}} \qquad (1)$$

where the E^* is the equivalent Young's Modulus and R^* is the equivalent radius. They are defined as:

$$\frac{1}{R^*} = \frac{1}{R_i} + \frac{1}{R_j} \qquad (2)$$

$$\frac{1}{E^*} = \frac{\left(1 - v_i^2\right)}{E_i} + \frac{\left(1 - v_j^2\right)}{E_j} \qquad (3)$$

with E_i, v_i, R_i, and E_j, v_j, R_j being the Young's Modulus, Poisson's ratio, and radius of each sphere in contact. Additionally, a damping force, F_n^d is given by

$$F_n^d = -2 \sqrt{\frac{5}{6}} \beta \sqrt{S_n m^*} v_n^{rel} \qquad (4)$$

$$m^* = \left(\frac{1}{m_j} + \frac{1}{m_i}\right)^{-1} \qquad (5)$$

where m^* is the equivalent mass and v_n^{rel} is the normal component of the relative velocity. The β (damping ratio) and S_n (normal stiffness) are defined as

$$\beta = \frac{-\ln e}{\sqrt{\ln^2 e + \pi^2}} \qquad (6)$$

$$S_n = 2E^* \sqrt{R^* \delta_n}. \qquad (7)$$

The constant e is the coefficient of restitution. The tangential force, F_t, depends on the tangential overlap δ_t and the tangential stiffness S_t

$$F_t = -S_t \delta_t \qquad (8)$$

$$S_t = 8G^* \sqrt{R^* \delta_n} \qquad (9)$$

where G^* is the equivalent shear modulus. Additionally, tangential damping force is defined as

$$F_t^d = -2 \sqrt{\frac{5}{6}} \beta \sqrt{S_t m^*} v_t^{rel} \qquad (10)$$

where v_t^{rel} is the relative tangential velocity. The tangential force is limited by Coulomb friction, $\mu_s F_n$, where μ_s is the coefficient of static friction. The rolling friction (Sakaguchi et al., 1993) is implemented by applying torque

$$\tau_i = -\mu_r F_n d_i \Omega_i \qquad (11)$$

to the contacting objects, where μ_r is the coefficient of rolling friction, d_i is the distance of the i-th contact point from the center of mass, and Ω_i is the unit angular velocity vector of the object at the contact point. The Hertz-Mindlin contact model with JKR cohesion (Johnson et al., 1971) allows modelling of cohesive materials. It calculates the normal force as a function of overlap δ_n and the surface energy parameter γ as follows:

$$F_{JKR} = -4 \sqrt{\pi \gamma E^*} a^{3/2} + \frac{4E^*}{3R^*} a^3, \qquad (12)$$

$$\delta_n = \frac{a^2}{R^*} - 2 \sqrt{\frac{\pi \gamma a}{E^*}} \qquad (13)$$

where E^* is the equivalent Young modulus, a is contact overlap radius, and R^* is the equivalent radius from Eq. 2. Wheel slip and circumferential velocity were used as an initial condition to each system. Wheel slip is defined as:

$$i = 1 - \frac{v_f}{\omega r} \qquad (14)$$

Eq. 14 defines wheel slip i in terms of the wheel forward velocity v_f, wheel angular speed ω, and wheel radius $r = D/2$. Post-processing values such as net traction and gross traction were calculated using Eq. 15 and Eq. 16, respectively.

$$F_x = \sum_j F_x^j \qquad (15)$$

$$T = \frac{1}{r} \sum_j F_t^j d_j \qquad (16)$$

F_x is the forward component of the contact force, F_t is the wheel-surface-tangential component of the contact force, D is the wheel diameter and d_j is distance from the contact point to the wheel axis. F_t has negative/positive sign if the force acts to increase/decrease wheel rotation. The sum in Eq. 16 represents the torque exerted on the wheel by soil contacts forces. Sinkage amount was based on the settled height of the soil surface.

3. Simulation methodology

The wheel, weighting 980 N, was placed −1.3 meters away from the center of the bed. By coupling a driving program to EDEM, the wheel was then displaced at a constant circumferential velocity of 97.6 mm/s and with a forward velocity matching the desired slip to the final position of 1.3 m from the bed center. With one degree of freedom, the wheel only moved freely along the vertical direction (allowing sinkage). Fig. 3 shows the initial configuration of the system. Fig. 4 shows a final state of a system with sinkage. For both figures, particles are colored according to their vertical position relatively to the box center. Color range is zoomed-in to near-surface locations to improve visualization of the surface deformation and sinkage.

Simulations with prescribed wheel slip values between −5.9% and 54.8% following the physical experiments by Shinone et al. (2010) were performed at constant simulation time step of 2.07×10^{-5}, which is 5% of Rayleigh Time Step. Net traction, gross traction, and wheel sinkage were calculated and plotted at each time step. Fig. 5 shows plots of these values over the simulation span for material number 1636 at 54.8% wheel slippage. Data outliers near $t = 0$ s are due to the wheel being dropped into the soil from above the soil surface.
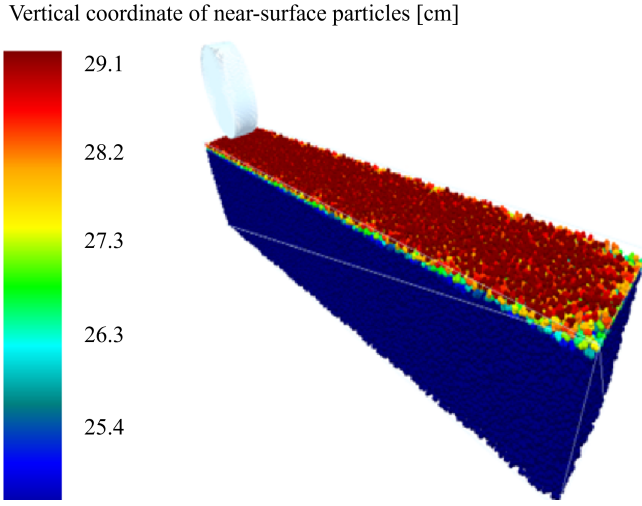
Vertical coordinate of near-surface particles [cm]

Figure 3: Initial position of the wheel in the particle bed
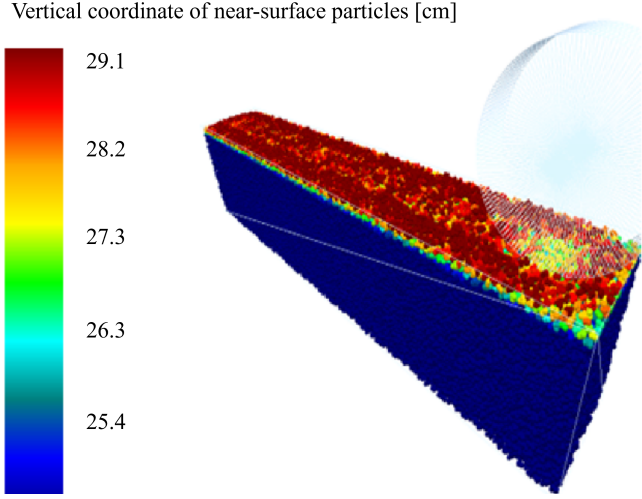

Vertical coordinate of near-surface particles [cm]

Figure 4: Final position of the wheel in the particle bed: GEMM 1636, 54.8% slippage

4. Comparison of DEM predictions with lab measurements

Figures 6 and 7 show averaged net and gross traction vs. slip curves from simulations along with lab measurements from (Shinone et al., 2010). Similarly, Fig. 8 shows wheel sinkage calculated from the lowest point of the wheel and the settled height of the particle bed. Data outside the distance interval of −1 m to 1 m was excluded from average calculation to avoid artifacts from the box boundaries and from the wheel being dropped.

Coefficient of determination, R^2, as defined by Eq. 17, was calculated to quantitatively assess how well the DEM results fit the experimental data.

$$R^2 = 1 - \frac{\sum (y_i - \hat{y}_i)^2}{\sum (y_i - \bar{y})^2} \qquad (17)$$

R^2 is the function to obtain the correlation between prediction and experiment, with y_i representing the experimental data and
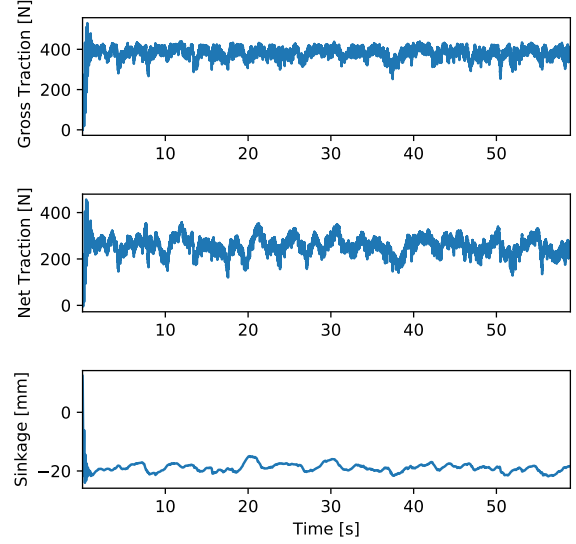

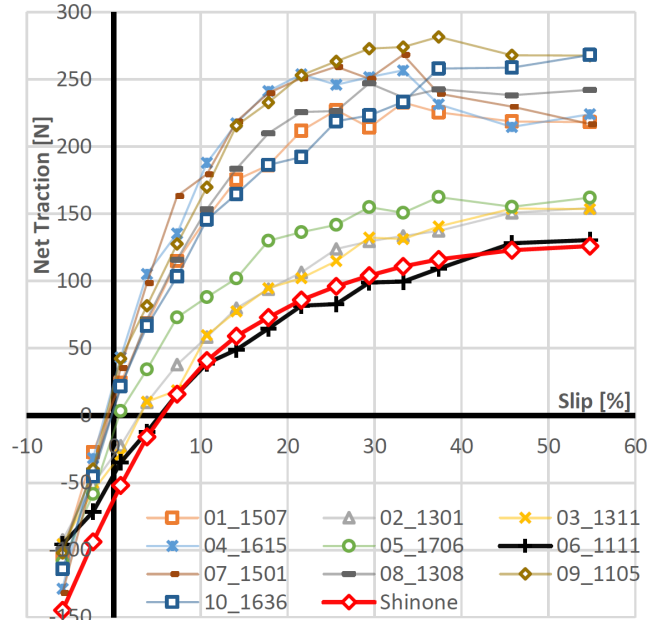Figure 5: Sinkage, Net Traction, and Gross Traction versus time: GEMM 1636, 45.8% slippage

Figure 6: Net tractive effort (drawbar pull)

$\hat{y}_i$ representing the data obtained through DEM. $\bar{y}$ is the mean of the experimental dataset.

Table 3 shows the R^2 values for net traction, gross traction, and sinkage from DEM when compared to the data from Shinone et al. (2010). R^2 values close to 1 show the best correlation, while most-negative R^2 values show worst correlation.

Overall, the gross tractive effort was best matched, on average, by selected DEM materials, followed by the net traction and sinkage. The materials with JKR cohesion (1507, 1615, 1501, 1308, and 1105) and materials with non-zero particle-particle rolling friction (1706) yielded the worst match and were
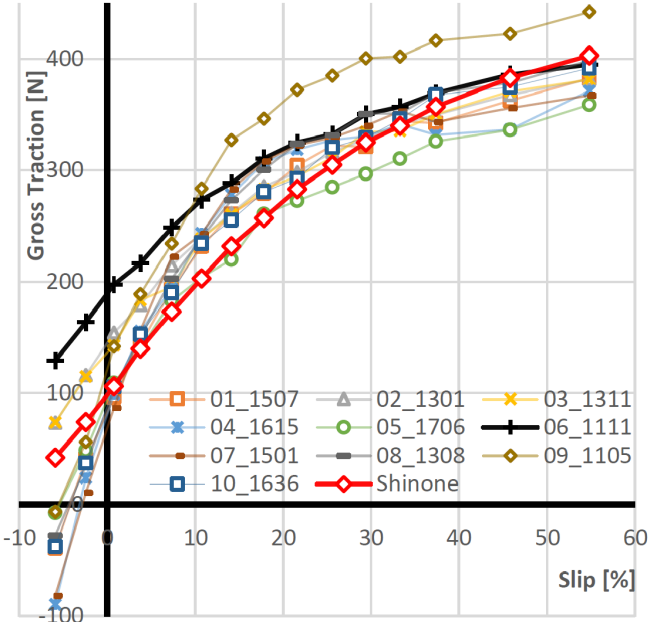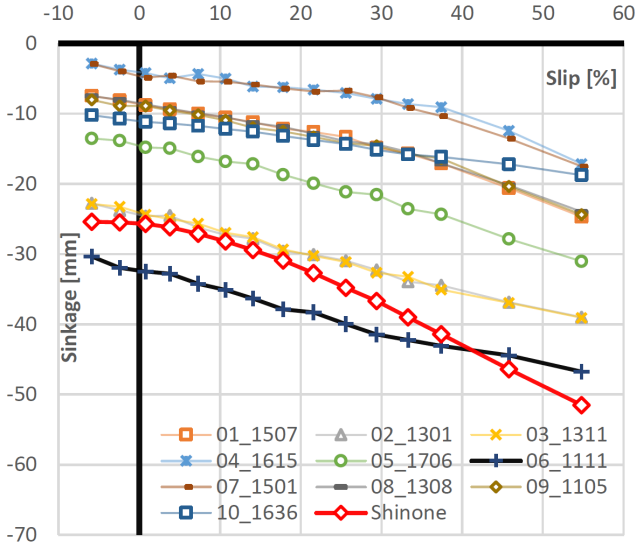
Figure 7: Gross tractive effort

Table 3: R^2 values of DEM vs. Shinone data

Material	Net Traction	Gross Traction	Sinkage
01_1507	-0.5590	0.9342	-5.8022
02_1301	0.8787	0.9327	0.5885
03_1311	0.8959	0.9451	0.5947
04_1615	-1.4183	0.8245	-10.4610
05_1706	0.6805	0.9424	-2.1570
06_1111	0.9616	0.7279	0.4948
07_1501	-1.5219	0.8165	-10.1685
08_1308	-0.9012	0.9152	-5.8888
09_1105	-1.8150	0.6524	-5.6872
10_1636	-0.7236	0.9410	-5.7698

study. The coarse scale of the particles presumably interferes with tractive response by preventing as much sinkage as seen in the experiments done by Shinone et al. (2010), except for material 1111 with low particle-particle static friction coefficient. With additional effort, particle size can be calibrated to better match experimental data using methods such as density scaling (Senatore et al., 2013). The relationship of size of the particles used for the coarse-scale DEM models can't be determined without preforming test simulations with different particle sizes, which is time intensive and beyond the goals of this study.

5.2. JKR cohesion

Subsets of DEM materials best matching the measurements of net traction, gross traction, and sinkage are shown in Fig. 9. Material models with JKR cohesion were initially used to test all materials that fell within the bulk density and angle of repose of our search, with test results shown in Figures 6–8. Doing so provides a reference point for cohesive materials and the impact of cohesion parameters on the simulation. From this data it was determined that the addition of cohesive parameters in the material model has an overall negative effect on matching lab results for dry sand, leading to the removal of materials with $\gamma \neq 0 \text{ J/m}^2$ from any additional work.

5.3. Parameter effects on net traction

A best-to-worst order of net traction match for non-JKR DEM materials is 1111, 1311, 1301, 1706, and 1636, given by the R^2 values of 0.9616, 0.8959, 0.8787, 0.6805, and -0.7236. Materials 1301 and 1311 have similar parameters, differing only in particle-particle coefficient of restitution e_p being 0.15 for material 1301 and 0.55 for 1311. Each of the net traction, gross traction, and sinkage responses from these two materials are nearly identical, therefore material response for the subset of parameters examined in this study is not sensitive to e_p. The best net traction match is obtained from material 1111. Material 1111 has particle-particle static friction coefficient $\mu_s^p = 0.44$ which is lower than 0.68 for materials 1301 and 1311. Observing net traction in Fig. 9 (a) leads to a conclusion that increasing μ_s^p increases the net traction, with larger increase for larger slip ratios. This claim is supported by the next best net traction

Figure 8: Sinkage

excluded from further study.

5. Discussion of effects of DEM parameters on material responses

Next we will analyze the sensitivity of DEM material response to changes in DEM model parameters.

5.1. Particle size

The smallest particle size available in the GEMM database, resulting in mean particle radius of 9.5 mm, was chosen in this
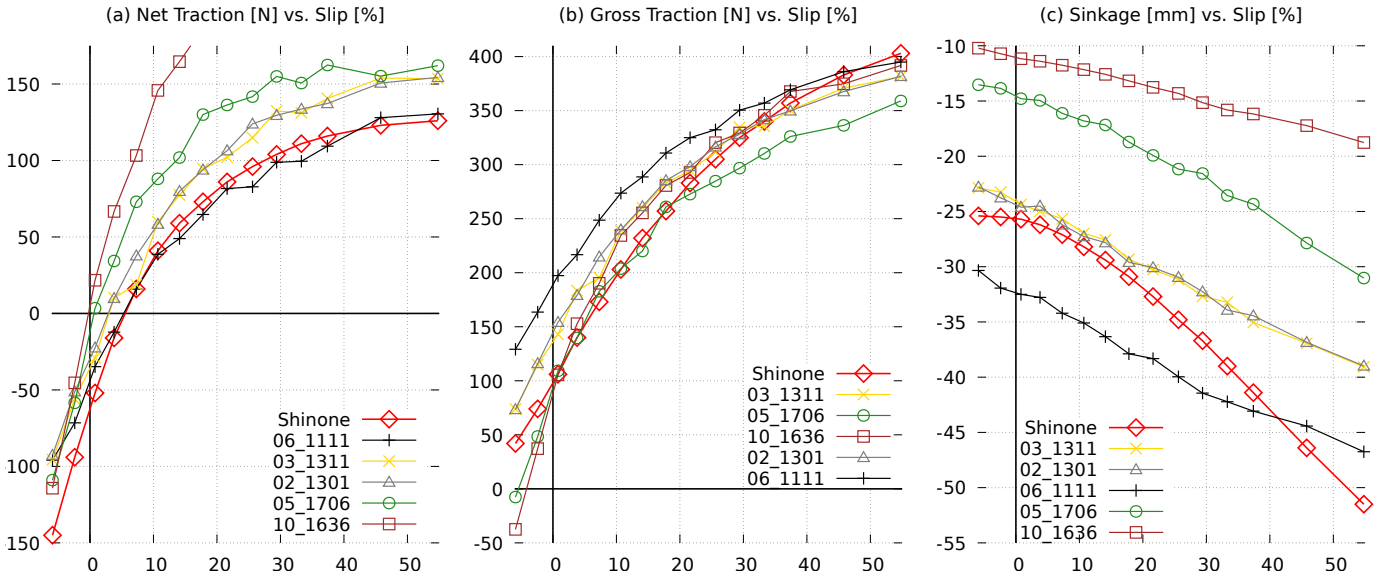
Figure 9: DEM materials best matching measured data. DEM material order in the legend starts from the best match.

match, material 1706, which has particle-particle static friction further increased (1.16), resulting in further increased net traction values, except for the two largest slips where the net traction from material 1706 is similar to materials 1301 and 1311. Material 1636 shows the worst net traction agreement with the experimental data, exhibiting too high net traction. The high net traction of the material 1636 can be attributed to 1636 being the only material with non-zero particle-particle rolling friction coefficient ($\mu_r^p = 0.05$), resulting in low sinkage magnitude. Overall, rise in net traction in Fig. 9 (a) correlates very well with decrease in sinkage magnitude in Fig. 9 (c).

5.4. Parameter effects on gross traction

A best-to-worst order of gross traction match for non-JKR DEM materials in terms of R^2 values is 1311 (0.9451), 1706 (0.9424), 1636 (0.9410), 1301 (0.9327), and 1111 (0.7279), with all materials except 1111 giving R^2 greater than 0.9. The material responses are shown in Fig. 9 (b). In a trend opposite to net traction, the increase in static particle-particle friction results in lowering the gross traction, as can be seen in progression for materials 1111 (0.44), 1301 (0.68) and 1311 (0.68), and 1706 (1.16). Introduction of non-zero particle-particle rolling friction coefficient in material 1636, as compared to material 1706 with similar parameters, significantly lowered the gross traction at high slip values, which can be correlated with significantly lower sinkage magnitude in Fig. 9 (c).

5.5. Parameter effects on sinkage

For sinkage, the best-to-worse R^2 values are obtained from non-JKR DEM materials 1311 (0.5947), 1301 (0.5885), 1111 (0.4948), 1706 (-2.1570), and 1636 (-5.7698). These material responses are shown in Fig. 9 (c). The increase in particle-particle static friction coefficient, as can be seen in progression for materials 1111 (0.44), 1301 (0.68) and 1311 (0.68), and 1706 (1.16), lowered the magnitude of sinkage. Non-zero

particle-particle rolling friction coefficient for material 1636 lowered the sinkage magnitude even more, especially for large slip values.

Sinkage prediction has the largest mismatch when compared to experimental results. Also, the trend of sinkage vs. slip curve leveling up at negative slips observed in soil-bin measurements is not captured by DEM. Authors attribute this to large particle size. However, for sinkage values lower than 10% of wheel diameter, the accuracy of net and gross traction may be considered more important than matching sinkage.

6. Conclusions and future work

Comparison of DEM-model-predicted net traction, gross traction, and sinkage with lab-test net traction results reported by (Shinone et al., 2010) for a wheel in sand under varying slip conditions was performed using ten coarse-scale DEM materials selected from Altair®'s EDEM™ Generic Material Model (GEMM) database by matching the bulk density and angle of repose for dry sand.

It was found that, overall, the gross tractive effort was matched best by the DEM materials, followed by the net traction, while the sinkage was matched with lowest accuracy. The materials with JKR cohesion were giving the worst match and were excluded early in the study. Another parameter that was found to degrade accuracy was non-zero particle-particle rolling friction coefficient.

GEMM material 1111 provided the best agreement with lab test net traction results reported by (Shinone et al., 2010). The net traction from material 1111 matched the lab test results with a coefficient of determination $R^2 = 0.96$, predicting slightly higher-than-experimental values at negative slips. For all materials except 1111, the net traction was overpredicted. The largest overpredictions of net traction were observed for DEM

materials with JKR cohesion and for the GEMM material 1636 with non-zero particle-particle rolling friction coefficient.

The gross traction predicted by DEM models for large positive slips agreed well with lab results, except for materials with non-zero JKR cohesion. The best fit to gross traction was obtained from GEMM material 1311 ($R^2 = 0.94$). The best gross traction agreement with lab results was observed for slips larger than 40%, resulting in an error lower than 5%. The agreement with lab results was worse at low positive and at negative slips. At the most negative slip (-5.9%), the gross traction was overestimated by up to 200% by GEMM material number 1111 and underestimated by approximately 200% by material 1636.

The best prediction for sinkage was obtained from GEMM material number 1311. This material matched the lab sinkage data with the coefficient of determination $R^2 = 0.59$, leading to conclusions that DEM materials examined in this study predict sinkage with lower accuracy than net and gross traction. For material 1311, the sinkage magnitude prediction is most accurate (less than 5% underestimation) for the slips around 10%. The largest sinkage-prediction error for this material was the sinkage underestimated by up to 27% for the largest slips, while the sinkage magnitude was underestimated by up to 10% for most-negative slips.

In the future, further parameter calibration could improve the accuracy of these models. However, doing so will require multiple iterations of material improvements and testing, and smaller particles would lead to increased computational costs.

7. Acknowledgements

8. Declaration of competing interest

The authors declare that they have no known competing financial interests or personal relationships that could have appeared to influence the work reported in this paper.

Appendix A.

References

Coetzee, C., 2017. Review: Calibration of the discrete element method. Powder Technology 310, 104–142.

Coetzee, C., 2020. Calibration of the discrete element method: Strategies for spherical and non-spherical particles. Powder Technology 364, 851–878.

De Pue, J., Cornelis, W.M., 2019. DEM simulation of stress transmission under agricultural traffic Part 1: Comparison with continuum model and parametric study. Soil and Tillage Research 195, 104408.

Table A.4: Nomenclature

Symbol	Value	Units
a	Contact radius	[m]
B	Box width	[m]
D	Wheel diameter	[m]
d_i	Distance of the i-th contact point from the center of mass	[m]
d_j	Distance from j-th particle wheel contact point to wheel axis	[m]
e	Coefficient of restitution	[]
E	Young's modulus	[Pa]
F^d	Damping force	[N]
F_G	Wheel weight	[N]
F_t	Tangential component of contact force	[N]
F_n	Normal component of contact force	[N]
F^x	Forward component of force on wheel	[N]
G	Shear modulus	[MPa]
H	Box depth	[m]
h	Soil depth	[m]
i	Wheel slip	[]
L	Box length	[m]
m	Mass	[kg]
N	Number of particles	[]
R	Hertz-Mindlin radius	[m]
R_i	Radius of a sphere in contact	[m]
r	Wheel radius	[m]
S	Stiffness	[N/m]
T	Gross tractive effort	[N]
v_f	Forward component of wheel velocity	[m/s]
v_n^{rel}	Relative velocity, normal component	[m/s]
v_t^{rel}	Relative velocity, tangential component	[m/s]
W	Wheel width	[m]
β	Damping ratio	[]
γ	JKR surface energy parameter	[J/m^2]
δ	Overlap	[m]
μ	Coefficient of friction	[]
μ_s	Coefficient of static friction	[]
μ_r	Coefficient of rolling friction	[]
ν	Poisson's ratio	[]
ω	Angular speed	[rad/s]
Ω_i	Unit angular velocity at i-th contact	[rad/s]
ρ	Solid density (material without voids)	[kg/m^3]
τ_i	Rolling friction torque for i-th contact	[Nm]

De Pue, J., Di Emidio, G., Verastegui Flores, R.D., Bezuijen, A., Cornelis, W.M., 2019. Calibration of DEM material parameters to simulate stress-strain behaviour of unsaturated soils during uniaxial compression. Soil and Tillage Research 194, 104303.

De Pue, J., Lamandé, M., Schjønning, P., Cornelis, W.M., 2020. DEM simulation of stress transmission under agricultural traffic Part 3: Evaluation with field experiment. Soil and Tillage Research 200, 104606.

Du, Y., Gao, J., Jiang, L., Zhang, Y., 2017a. Numerical analysis of lug effects on tractive performance of off-road wheel by DEM. Journal of the Brazilian Society of Mechanical Sciences and Engineering 39, 1977–1987.

Du, Y., Gao, J., Jiang, L., Zhang, Y., 2017b. Numerical analysis on tractive performance of off-road wheel steering on sand using discrete element method. Journal of Terramechanics 71, 25–43.

Du, Y., Gao, J., Jiang, L., Zhang, Y., 2018. Development and numerical validation of an improved prediction model for wheel-soil interaction under multiple operating conditions. Journal of Terramechanics 79, 1–21.

Altair Engineering, 2022. Altair Product Documentation. Altair

Engineering. `https://help.altair.com/EDEM/Creator/Creator_Tree-Physics.htm`.

Glover, T., 1997. Pocket ref. 2nd ed., Sequoia Publishing Inc.

Johnson, J.B., Duvoy, P.X., Kulchitsky, A.V., Creager, C., Moore, J., 2017. Analysis of Mars Exploration Rover wheel mobility processes and the limitations of classical terramechanics models using discrete element method simulations. Journal of Terramechanics 73, 61–71.

Johnson, J.B., Kulchitsky, A.V., Duvoy, P., Iagnemma, K., Senatore, C., Arvidson, R.E., Moore, J., 2015. Discrete element method simulations of Mars Exploration Rover wheel performance. Journal of Terramechanics 62, 31–40.

Johnson, K.L., Kendall, K., Roberts, A.D., 1971. Surface energy and the contact of elastic solids. Proceedings of the Royal Society of London. A. Mathematical and Physical Sciences 324, 301–313.

Knuth, M.A., Johnson, J.B., Hopkins, M.A., Sullivan, R.J., Moore, J.M., 2012. Discrete element modeling of a Mars Exploration Rover wheel in granular material. Journal of Terramechanics 49, 27–36.

Mindlin, R.D., Deresiewicz, H., 1953. Elastic Spheres in Contact Under Varying Oblique Forces. Journal of Applied Mechanics 20, 327–344.

Nakashima, H., Fujii, H., Oida, A., Momozu, M., Kanamori, H., Aoki, S., Yokoyama, T., Shimizu, H., Miyasaka, J., Ohdoi, K., 2010. Discrete element method analysis of single wheel performance for a small lunar rover on sloped terrain. Journal of Terramechanics 47, 307–321.

Nakashima, H., Kobayashi, T., 2014. Effects of gravity on rigid rover wheel sinkage and motion resistance assessed using two-dimensional discrete element method. Journal of Terramechanics 53, 37–45.

Recuero, A., Serban, R., Peterson, B., Sugiyama, H., Jayakumar, P., Negrut, D., 2017. A high-fidelity approach for vehicle mobility simulation: Nonlinear finite element tires operating on granular material. Journal of Terramechanics 72, 39–54.

Sakaguchi, H., Ozaki, E., Igarashi, T., 1993. Plugging of the Flow of Granular Materials during the Discharge from a Silo. International Journal of Modern Physics B 7, 1949–1963.

Senatore, C., Wulfmeier, M., Vlahinić, I., Andrade, J., Iagnemma, K., 2013. Scaling of discrete element model parameters for cohesionless and cohesive solid. Journal of Terramechanics 223, 311–326.

Shinone, H., Nakashima, H., Takatsu, Y., Kasetani, T., Matsukawa, H., Shimizu, H., Miyasaka, J., Ohdoi, K., 2010. Experimental analysis of tread pattern effects on tire tractive performance on sand using an indoor traction measurement system with forced-slip mechanism. Engineering in Agriculture, Environment and Food 3, 61–66.

Šmilauer, V., et al., 2015. Yade Documentation 2nd ed. The Yade Project. Http://yade-dem.org/doc/.

Yang, P., Zang, M., Zeng, H., 2020. DEM–FEM simulation of tire–sand interaction based on improved contact model. Computational Particle Mechanics 7, 629–643.

Zeng, H., Xu, W., Zang, M., Yang, P., 2020a. Calibration of DEM-FEM model parameters for traction performance analysis of an off-road tire on gravel terrain. Powder Technology 362, 350–361.

Zeng, H., Xu, W., Zang, M., Yang, P., Guo, X., 2020b. Calibration and validation of DEM-FEM model parameters using upscaled particles based on physical experiments and simulations. Advanced Powder Technology 31, 3947–3959.